Twin-entry turbine losses: an analysis using CFD data.

José Galindo[1], José Ramón Serrano[1], Luis Miguel García-Cuevas[1] and Nicolás Medina[1]

Abstract

The current paper presents a computational fluid dynamics (CFD) flow behaviour and losses analysis of twin-entry radial turbines in terms of its Mass Flow Ratio (*MFR*, the ratio between the flow passing through one of its intake ports and its total mass flow), focusing on the mixing phenomena in the unequal admission conditions cases. The CFD simulations are first validated with experimental data. Then, the losses mechanisms are analysed and quantified in the different parts of the twin-entry turbine in terms of the *MFR* value. A sudden expansion is found at the junction of both branches in the interspace between volutes and rotor for unequal and partial admission cases. Tracking the flow coming from each of the turbine intake ports, it has been observed that both flow branches do not fully mix with each other within the rotor. Another source of losses has been identified in the contact between both flow branches due to their momentum exchange that depends on the difference between both flow branches velocities. These losses have not been considered before, and they should be included in mean line loss-based models for twin-entry turbine since they are very significant for unequal admission conditions.

Keywords

Turbocharger, Twin-entry turbine, CFD analysis, Losses, Entropy Generation

[1]CMT – Motores Térmicos. Universitat Politècnica de València, Spain

Corresponding author:
Nicolás Medina, CMT – Motores Térmicos. Universitat Politècnica de València, Valencia, Spain.
Email: nimeto@mot.upv.es

1 Introduction

The emission standards in internal combustion engines (ICE) are becoming increasingly stringent all around the world, especially for passenger car vehicles, as in the European Union with the Euro 6 [1], in China with the China 5 and China 6 [2], in the United States of America with the Tier 3 [3] or in India with the Bharat Stage 6 [4].

Since the computational power has increased exponentially, computational fluid dynamics (CFD) simulations have become a fundamental solution that complements the experimental measurements for studying some engine phenomena that allow to reduce these emissions. Very different phenomena can be simulated, as heat transfer models [5], turbocharger unsteady behaviour prediction [6], internal details of fuel injectors [7], URANS/LES cylinder simulations [8, 9] or noise characterisation [10, 11].

One of the most wide and efficient techniques for reducing the emissions is turbocharging the ICE [12]. The engine exhaust turbine configuration most used until relatively recently was the single volute turbine. However, having only one volute in multiple cylinder engines may create interference problems, as described by Garret et al. [13]. The pulsating flow coming from cylinders of adjacent firing order produces these interferences. It damages the cylinder scavenging process, increasing engine back flows, trapped residuals and reduce the volumetric efficiency. These drawbacks can be reduced by using turbines with multiple entries, with each entry connected to exhaust ports of different cylinders. The most typical and simple solution is the twin-entry turbine, that has two volutes meridionally separated. The pulses coming from adjacent firing order cylinders are connected to different volutes, so they are better isolated and their interferences are reduced. Despite these improvements, some new phenomena arise in the space after the union of both volutes that must be taken into account. Numerous authors have experimentally characterised twin-entry turbines focusing on the blade loading loss in the rotor as Aghaali and Hajilouy-Benisi [14], the acoustic response as Serrano et al. [15], the swallowing capacity as Romagnoli et al. [16], the effect of integrating a balance valve as Jin et al. [17] or the unequal admission conditions as Brinkert et al. [18].

Other authors have carried out a loss analysis of twin-entry turbines using also CFD simulations. Yingxian et al. [19] simulated a twin-entry mixed flow nozzled turbine and they calculated the losses separately for

the volute, the nozzle and the rotor using loss coefficients based on the stagnation pressure for each part. They also analysed the incidence flow angles and the secondary flows in the nozzle and the rotor for partial admission conditions. However, they did not analyse these flow patterns when there are unequal admission conditions, which is the most common operation in real engines. Cerdoun and Ghenaiet [20] focused their twin-entry turbine pulsating CFD analysis on the phenomena at the volutes and the interspace between volutes and rotor, describing the formation of secondary flows at extreme admission conditions due to the swirling motion.

These studies [19, 20] show their results in terms of pressure ratio and efficiency. In the current paper, an analysis in terms of Mass Flow Ratio (*MFR*) is presented. The *MFR* is defined in Eq. 1. It relates the mass flow passing through the shroud branch and the total mass flow passing through both shroud and hub branches. Other authors have used similar parameters such as Chiong et al. in [21]. However, the *MFR* parameter has shown good correlation with important variables of the one-dimensional models such as the rotor inlet and outlet areas or the rotor inlet incidence angle, as described by Galindo et al. [22]. It allows to perfectly differentiate the mass flow admission conditions. Thus, the flow behaviour at unequal admission conditions can be properly understood.

$$MFR = \frac{\dot{m}_{\mathrm{s}}}{\dot{m}_{\mathrm{s}} + \dot{m}_{\mathrm{h}}} \tag{1}$$

This flow analysis in terms of *MFR* helps to better understand the mixing phenomena in the interspace between volutes and rotor and inside the rotor of twin-entry turbines at unequal admission conditions. It is also useful for quantifying the different losses along the twin-entry turbine and to discern which are their sources. This information can be valuable for readers that research on twin-entry turbines and wish to develop mean line losses models. In concrete, future works of authors will be devoted to build such reduced order model and to improve the one-dimensional loss-based models proposed by Serrano et al. [23, 24]. It could also be coupled with other turbocharger sub-models as the compressor quasi-steady map extrapolation [25] or the one-dimensional wave and mass accumulation effects [26].

In the following sections, the experimental campaign is first described. Then, the CFD set-up is explained and the simulations globally validated

against experimental data. Then, the flow analysis in terms of *MFR* is carried out for quantifying the twin-entry turbine pressure losses focusing on the mixing phenomena. Finally, the main conclusions of this study are presented.

2 Experimental campaign

The turbine map was measured in a gas stand described by Serrano et al.[27] and shown schematically in Fig. 1. In this gas stand, pressurized air is produced in a two-stage radial compressor and fed to both twin-turbine intake ports through two independent ducts.

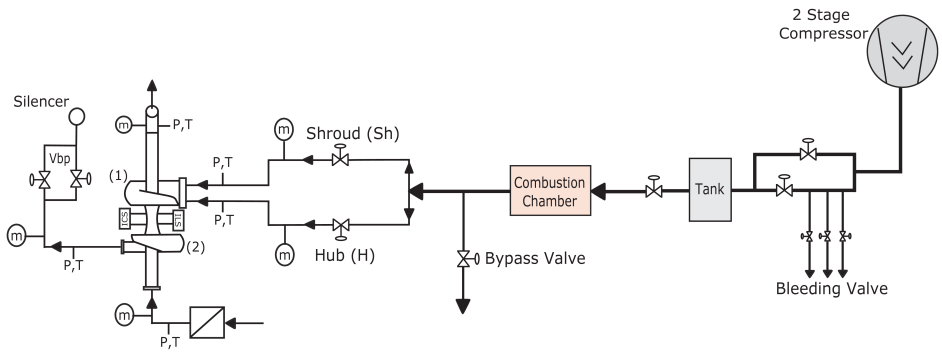

Figure 1. Gas stand used to measure the turbine map, from Serrano et al.[27].

The inlet total pressure and mass flow is controlled independently for each turbine entry by means of two controlled valves. The turbine power output is consumed by the friction losses of the system and by a radial compressor attached to it, which operating point can be controlled by means of a back-pressure valve.

The rotational speed of the turbocharger is measured by means of an inductive sensor and there are measurement stations for the flow pressure and temperature at both turbine inlets, turbine outlet, compressor inlet, and compressor outlet. For measuring these temperatures, an array of four type-K thermocouples was used in each measurement station, whereas several piezoresistive sensors were used for measuring the pressure. The mass flow rate of the compressor is measured by means of a thermal flow

Table 1. Uncertainty of the different turbine variables.

Parameter	Average uncertainty	Maximum uncertainty	Units
Temperature	0.47	0.47	K
Mass flow	203	252	$\mathrm{mg\,s^{-1}}$
Pressure	7.3	7.3	hPa
Rotational speed	500	500	rpm
Reduced speed	3.7	4.7	$\mathrm{rpm\,K^{-0.5}}$
Expansion ratio	0.015	0.023	-
Apparent efficiency	0.020	0.049	-
Power	95	216	W
Reduced mass flow	3.45×10^{-8}	6.32×10^{-8}	$\mathrm{m\,s\,K^{0.5}}$
MFR	0.0017	0.0054	-

meter. The mass flow of both turbine inlets and outlet ducts are measured by means of differential pressure V-cone sensors. The uncertainty of the different variables, both directly measured and computed, is shown in Table 1.

A total of 233 steady-state turbine working points were measured, for *MFR* values ranging from 0 to 1 and reduced speeds going from $3700\,\mathrm{rpm\,K^{-0.5}}$ to $7400\,\mathrm{rpm\,K^{-0.5}}$.

3 CFD Set-up

The twin-entry turbine geometry used for the 3D CFD simulations is shown in Fig. 2a. The computer-aided design (CAD) model employed, which reconstruction is explained in Galindo et al. [22], is shown in Fig. 2b. Its main geometrical parameters are summed up in Table 2 along with data about the engine on which this twin-entry turbine is used.

Since the geometry is complex, the chosen mesh is a non-structured polyhedral mesh with prism layer mesher for capturing well the regions near the walls. This mesh is more refined in the regions where more complex physics phenomena arise as the rotor tip clearances. To ensure valid results, a mesh independence study has been carried out. As shown in Table 3, the total pressure at the rotor inlet, the efficiency, the torque and the reduced mass flow rate have been checked with the same boundary conditions but changing the mesh size. The case simulated with different

(a) Twin-entry turbine.

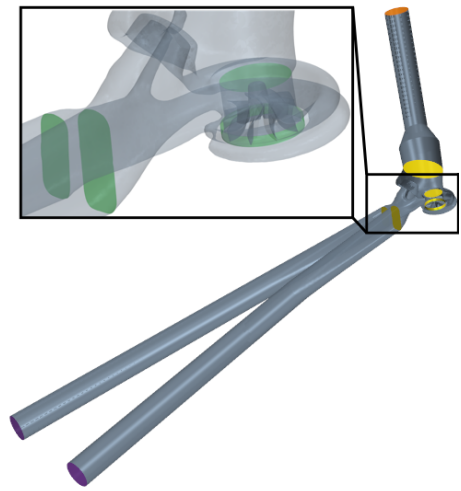

(b) Twin-entry turbine CAD model and CFD domain.

Figure 2. Geometry

mesh sizes has an *MFR* equal to 0.53 and a reduced turbocharger speed of $3700\,\mathrm{rpm\,K^{-0.5}}$.

The mesh dependency study is carried out for reaching a compromise between results precision and computational cost. The results precision required in the current work is smaller than the experimental uncertainty of the data used for validating the simulations. From Table 3, the best option is to choose the mesh with 5.5 million cells since the results obtained are very close to the case with 8.28 million cells and are less computationally expensive. This final chosen mesh is presented in Fig. 3. At the bottom line of Table 3, the global order of accuracy (GOA) and the global convergence index (GCI) of the total pressure at the rotor inlet, the efficiency, the torque and the reduced mass flow has been computed. The GOA takes

Table 2. Twin-entry turbine geometrical parameters and engine parameters on which this turbocharger is used.

Parameter	Value
Rotor inlet diameter [mm]	45.1
Rotor outlet diameter [mm]	40.9
Nut diameter [mm]	12.1
Number of blades	9
Blade inlet height [mm]	6.6
Blade inlet angle [deg]	0
Mean blade outlet angle [deg]	56
Mean blade thickness [mm]	1.2
Mean tip clearance [mm]	0.39
Engine type	Gasoline
Number of cylinders	4
Engine displacement [L]	2
Car segment	D

Table 3. Mesh independence study: variation of total pressure at rotor inlet, efficiency, torque and reduced mass flow rate.

N of cells ($\cdot 10^6$)	Total pressure [kPa]	η [-]	M [N $\cdot$ m]	$\dot{m}_{red}$ [$\frac{\mathrm{kg}\cdot\sqrt{\mathrm{K}}}{\mathrm{s}\cdot\mathrm{MPa}}$]
1.59	135.9	0.6888	0.2101	10.654
2.83	136.1	0.6979	0.2132	10.672
4.46	136.4	0.7034	0.2151	10.681
5.54	136.5	0.7040	0.2153	10.684
8.28	136.5	0.7041	0.2154	10.685
GOA	1.958	1.740	1.741	1.851
GCI (%)	0.05	0.08	0.08	0.07

into account the local order of accuracy of the numerical methods used for the advection and diffusion terms of the RANS equations, as well as the propagation and accumulation of errors outside the stencil due to grid shape effects. This leads to a grid convergence index of less than 0.1% in all variables for the selected mesh, employing the method described by Roache [28]. This also matches the original required precision.

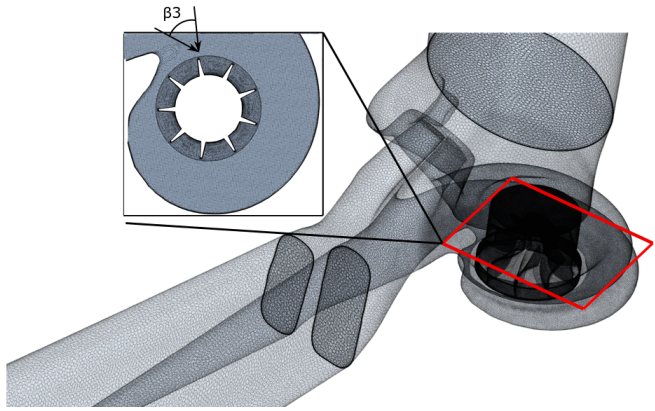

(a) General view of the mesh.

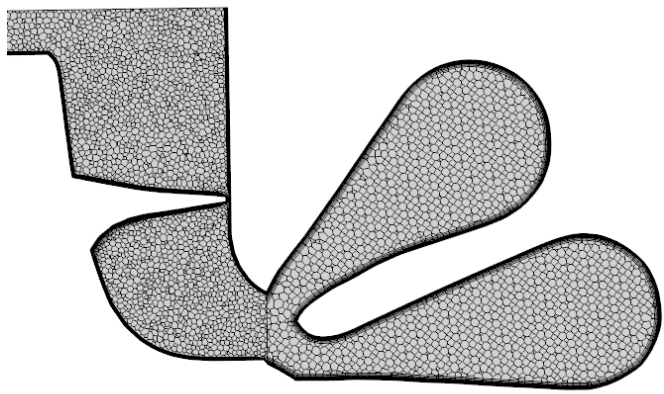

(b) Zoom at rotor and volutes mesh.

Figure 3. CAD model with final mesh.

The 3D CFD simulations of the current study are carried out using commercial software package Simcenter STAR-CCM+. The simulations use the unsteady Reynolds Averaged Navier-Stokes (URANS) for modelling the turbulence, solving the equations with an implicit, second order, upwind, coupled flow solver. Roe's flux-difference splitting scheme with Weiss-Smith preconditioning for all-speed flows is used. The turbulence model chosen is $k-\omega$ SST with compressibility correction and Durbin scale limiter for realizability. With the selected mesh, the non-dimensional distance to the centroid of the first layer of cells close

to the walls, Y^+, is calculated as < 2 for all the geometry. This value is reasonable for the models selected and should be able to capture the behaviour of the viscous sublayer of the boundary layer. Fig. 4 shows how the Y^+ at the rotor is always < 2.

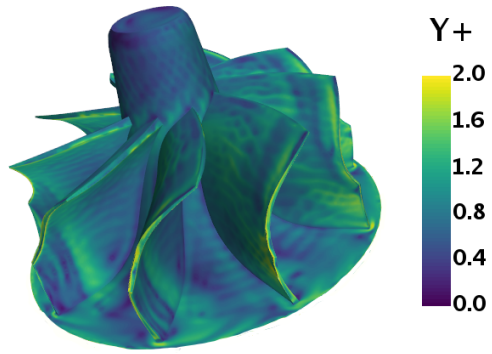

Figure 4. Y^+ value at the rotor.

The working fluid is air, computed as an ideal gas with temperature-dependent specific heat capacity and dynamic viscosity, as the experiments used for validating these simulations were performed with clean air. Moreover, the air passing through each turbine entry has been differentiated as hub air and shroud air respectively. Both fluids have the same exact gas properties, but the software allows the advection of these flows and tracking the concentration of each one locally using the passive scalar option. Therefore, the concentration of air coming from each branch can be followed along the geometry.

For simulating this twin-entry turbine, three different boundary conditions are needed. In the current work, all these boundary conditions are fixed values extracted from previous experimental data. For both entries of the turbine, the boundary conditions are defined as stagnation inlets where the total pressure, total temperature, turbulence description and gas composition are fixed. For the turbine outlet, the boundary condition is defined as a pressure outlet, where the static pressure, static temperature, turbulence description and gas composition are fixed. The temperature, turbulence parameters and gas composition of the outlet boundary conditions are only used in backflow situations, which merely appear during the transient phase of the simulations before achieving

convergence. Furthermore, the rotational speed of the rotor is set equal to that obtained from the experimental campaign.

At the beginning, the geometry is fixed using a moving reference frame for defining the rotor motion with a steady solver (RANS). This allows to achieve more realistic initial conditions for the unsteady solver. When the solution is converged, the solver is changed to an implicit unsteady solver (URANS) and the motion is defined using a rigid body motion. With rigid body motion, the rotor mesh rotates each time step of the simulation while the inlet and outlet meshes are fixed. The time step is constant and is calculated for each simulation as the time spent by the wheel in rotating one degree. This time step has been chosen following the study made by Galindo et al. [29]. In addition, twenty inner iterations are taken for each time step for ensuring the convergence of the results, while several parameters such as the residuals are also monitored during these inner iterations.

In the current work, four different turbocharger speeds are used for each of the nine different *MFR* values simulated, having a total of 36 cases simulated as shown in Table 4. These values are selected based on the experimental data already measured to be able to validate the simulations. Thus, the desired *MFR* values in the CFD simulations are obtained imposing the total pressure and total temperature experimentally measured in each branch inlet.

Table 4. Values of *MFR* and turbocharger reduced speed simulated.

MFR [-]	N_{red} [rpm/$\sqrt{\text{K}}$]
0	3700
0.2	4700
0.33	5800
0.43	7400
0.53	
0.57	
0.67	
0.8	
1	

These simulations have been globally validated with experimental results for both mass flow capacity map and apparent efficiency map.

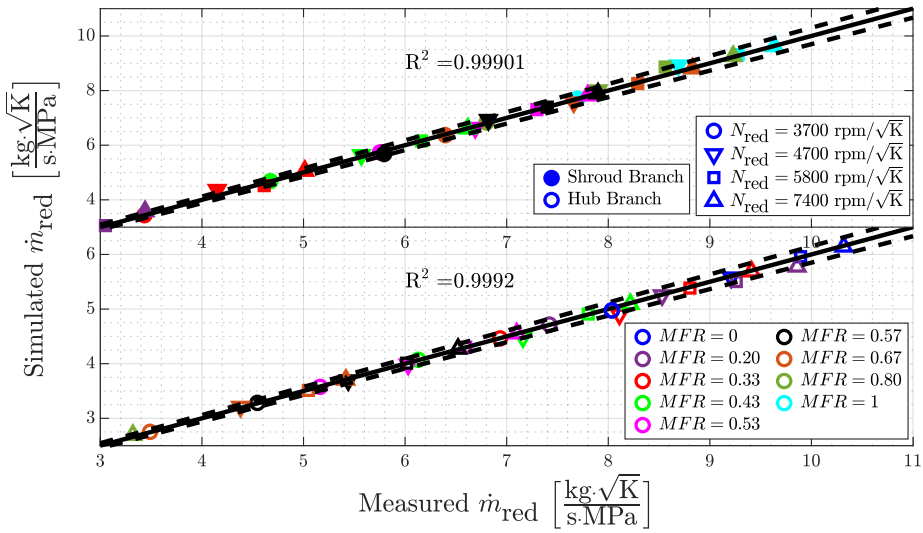

(a) Reduced mass flow rate.

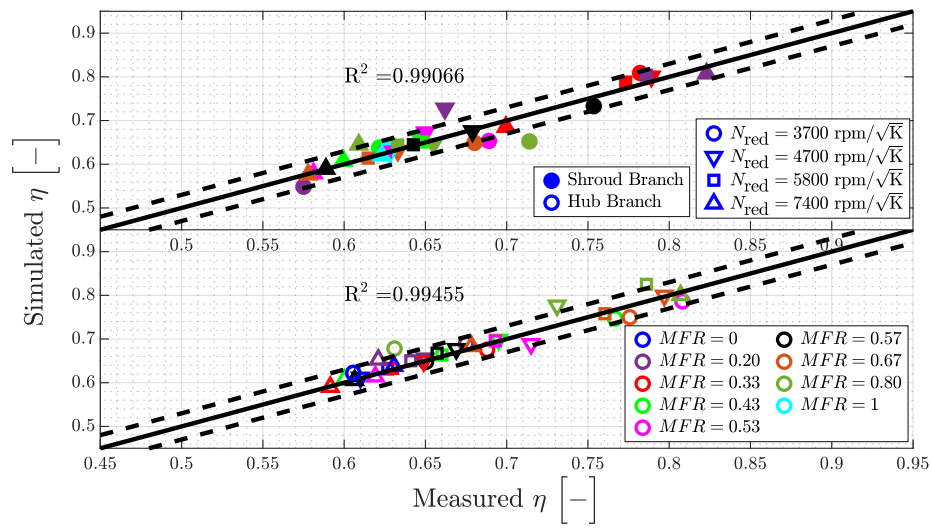

(b) Apparent efficiency.

Figure 5. Validation of computational simulations with experimental results.

The comparison of both experimental and computational results of reduced mass flow rate for the mass flow capacity map has an error lower

than 3% as shown in Fig. 5a. The comparison of apparent efficiency in both flow branches is also shown in Fig. 5b having an error lower than 5%.

Also, the comparison between CFD results and experimental measurements of the reduced mass flow rate to expansion rate map for both hub and shroud flow branches is shown respectively in Fig. 6a and Fig. 6b.

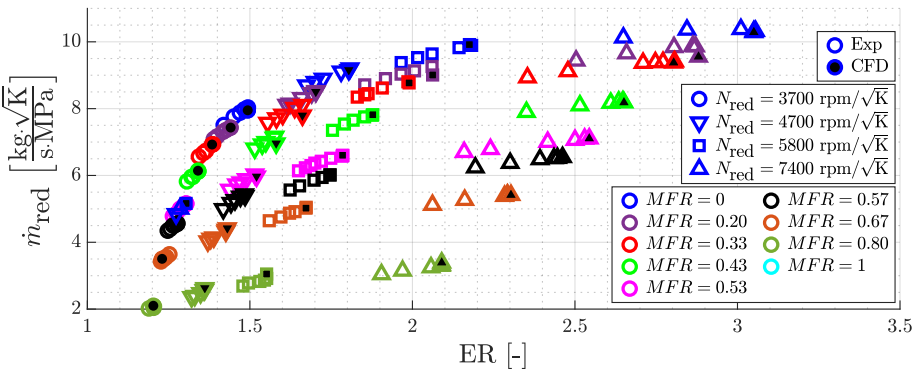

(a) Hub branch.

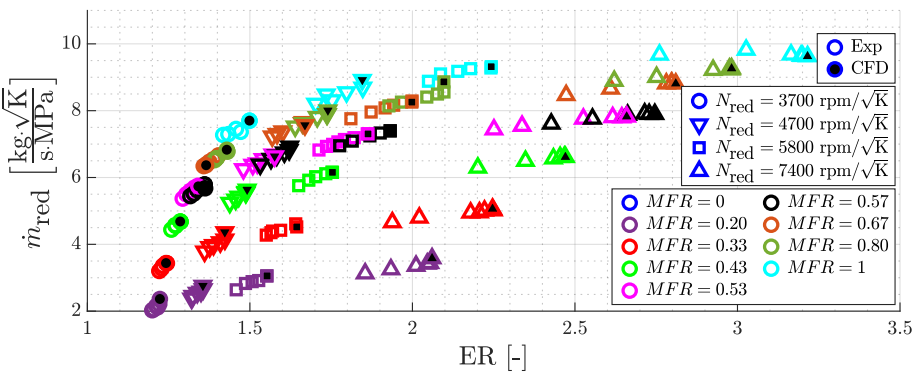

(b) Shroud branch.

Figure 6. Comparison between CFD results and experimental measurements of the mass flow rate to expansion rate map for both flow branches.

4 CFD Loss Analysis

Twin-entry turbines consist of four clearly differentiated parts: volutes, interspace between volutes and rotor, rotor and outlet. The current analysis is focused on losses due to the interaction between flow branches in the interspace and the rotor, but there is also a quantification of the main losses of all parts using the CFD results.

This analysis is carried out in terms of *MFR* and it demonstrates this variable has a significant influence in the different losses that exist in twin-entry turbines. Moreover, some of these losses depend directly on the *MFR* and they are quantified for each flow branch separately. In Galindo et al. [22], the authors studied twin-entry turbines as two separated single-entry turbines for the reduced-order model presented for the effective area. In that work, the rotor inlet and rotor outlet areas corresponding to each flow branch change lineally with the *MFR* value. Thus, the losses calculations presented in the current work are made applying these area variations.

4.1 Volute Losses

The volutes are the elements with closest to isentropic behaviour of the twin-entry turbines since there is no interaction between branches nor sudden expansions. There is also no mobile component inside of the volutes. The twin-entry turbine volutes are properly studied by other authors such as Cerdoun and Ghenaiet [20], so there will not be further flow analysis in this region.

For quantifying the volute losses, a reasonable approximation could be to use the passage losses model proposed by Futral et al. [30] and defined in Eq. 2 where ρ is the density, v the inlet absolute velocity and K a constant to be adjusted. Then, these losses can be compared with the pressure losses obtained from the CFD simulations. In the CFD simulations, the total pressure has been evaluated at the inlet and outlet areas of each volute for obtaining the total pressure losses.

$$\Delta p_{pass} = K \cdot \rho \cdot v^2 \tag{2}$$

Fig. 7 shows this quantification for the hub branch 7a and the shroud branch 7b respectively. The green bars represent the difference between the quantified total pressure losses and the total pressure losses obtained from the CFD simulations. The green bars under 0 mean that there is an over-prediction of the pressure losses, and the green bars over the passage

losses mean there is an under-prediction of the pressure losses. It can be observed that most of the effect is well captured with this model because it is the main source of losses and these differences are small in all cases.

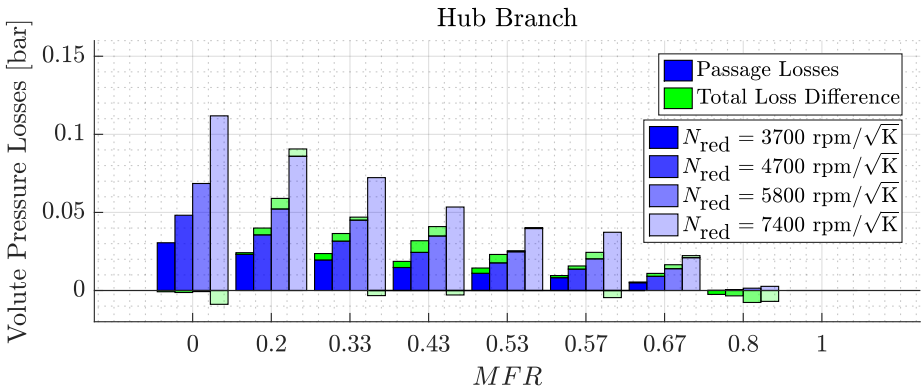

(a) Hub branch.

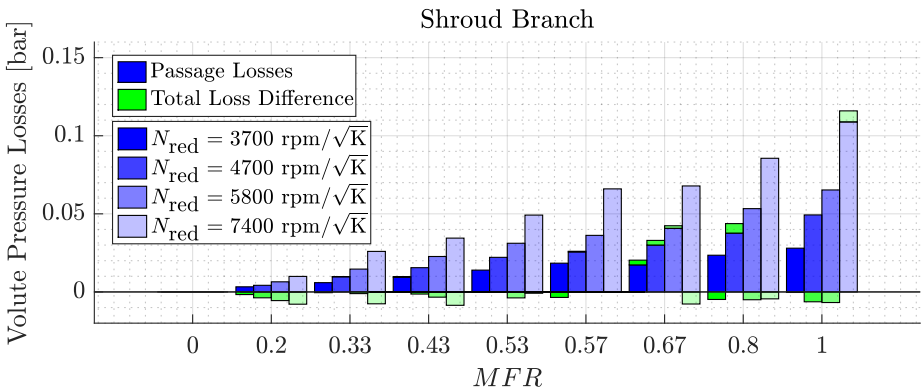

(b) Shroud branch.

Figure 7. Volute pressure losses quantification.

It can be noted that the pressure losses diminish from *MFR* 0 to 1 in the hub branch and from *MFR* 1 to 0 in the shroud branch. This is consistent with the reduction of mass flow and total inlet pressure when going from *MFR* equal to 0 to equal to 1 in the hub branch and from *MFR* equal to 1 to equal to 0 in the shroud branch.

4.2 Interspace Losses

Both flow branches are joined before the rotor inlet in the interspace, just after the volutes exit. Although being of a small volume, this space produces more complex phenomena than the volutes. Here, both flows join and there could be some losses due to this junction. Depending on the *MFR* value, there could be even a sudden expansion in the union if one of the branches has much more mass flow rate than the other one.

For *MFR* values near full admission conditions (in a range from 0.4 to 0.6), the main source of losses in the interspace is the friction with the walls. Since both flows have similar velocity and pressure conditions, the losses produced in their union are small.

Fig. 8a shows the entropy generation in a section of the interspace at 90° from the tongue for a case with an *MFR* equal to 0.53 and a reduced turbocharger speed of $4700\,\mathrm{rpm\,K^{-0.5}}$. It shows the wall friction is the main source of entropy generation in most interspace regions for cases with an *MFR* values near full admission conditions.

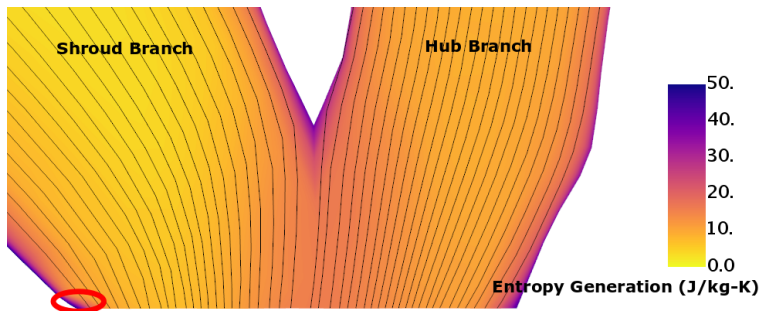

(a) Section at 90 degrees from the tongue.

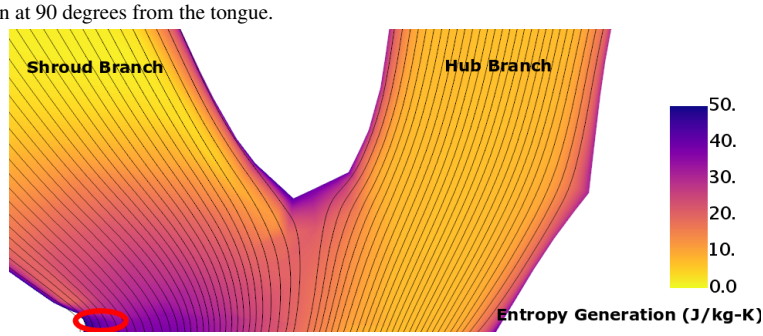

(b) Section at 15 degrees from the tongue.

Figure 8. Entropy generation in the interspace for an *MFR* equal to 0.53.

However, in the region near the tongue (sections at 0° to 30° from the tongue) there is an increment of entropy generation due to the junction between the incoming flow and the flow at section at 360° from the tongue. Fig. 8b shows the entropy generation in a section at 15° from the tongue where this effect is observed. The maximum entropy generation value for this case, $50\,\mathrm{J\,kg^{-1}\,K^{-1}}$, is marked in red in both sections.

For quantifying the losses due to the wall friction and the losses near the tongue in the interspace, a reasonable approximation is to use the passage losses model proposed by Futral et al. [30] defined in Eq. 2, as in the volute. The losses near the tongue can be included in this model adjusting the constant in Eq. 2 since they also depend on the flow conditions. With this model, the pressure losses in *MFR* values near full admission conditions are well captured, as it is shown in Fig. 9. However, it can be noted that for *MFR* values far from full admission conditions, there are discrepancies between the model and the total pressure losses. For *MFR* values lower than 0.4 in the hub branch 9a and higher than 0.6 in the shroud branch 9b, the model under-predicts the pressure losses. For *MFR* values higher than 0.6 in the hub branch 9a and lower than 0.4 in the shroud branch 9b, the model over-predicts the pressure losses. Hence, other physical phenomena have to be taken into account for capturing adequately the pressure losses in the interspace.

For *MFR* values lower than 0.4 in the hub branch and higher than 0.6 in the shroud branch, there is a sudden expansion at the junction of both volutes due to their different inlet pressures as shown in Fig. 10. The flow branch with greater pressure and mass flow rate tends to occupy more interspace volume than the flow branch with less pressure and mass flow rate, as detailed in [22]. Fig. 10 shows a section at 90° from the tongue in the interspace with velocity convolution lines for cases with *MFR* 0.67 10a and 0.20 10b, respectively. It shows the shroud air concentration, which is the local concentration of the gas entering the turbine through the shroud intake port. This sudden expansion can generate important pressure losses in these cases.

In extreme cases of *MFR*, like partial admission conditions, this sudden expansion can generate even bigger total pressure losses. Since there is no mass flow in the other branch, the flow can recirculate into the other volute limb when it arrives at the interspace. This recirculation generates great total pressure losses. Fig. 11 shows this recirculation in a case of

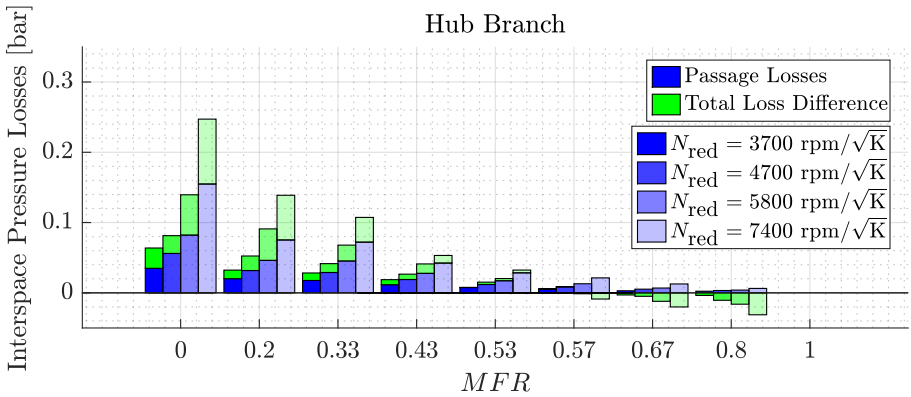

(a) Hub branch.

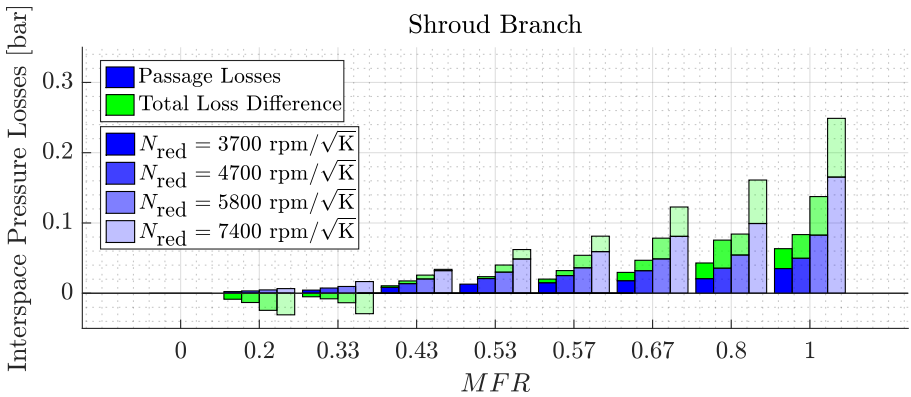

(b) Shroud branch.

Figure 9. Interspace passage losses quantification.

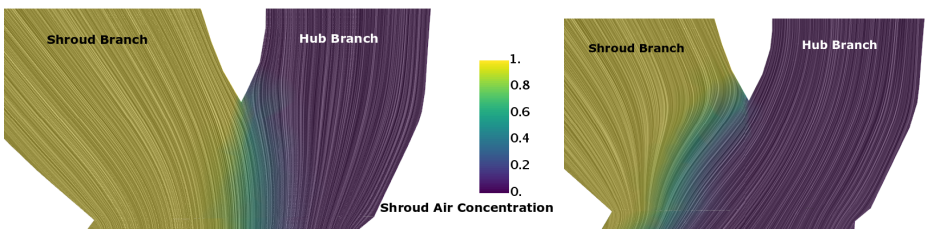

(a) *MFR* 0.67 **(b)** *MFR* 0.20

Figure 10. Interspace sudden expansion in a section at 90 degrees from the tongue.

MFR equal to 1 (all the entering the turbine through the shroud intake port) in a section at 90° from the tongue. A great entropy generation can be observed in the flow recirculated from the shroud branch to the hub branch, consistent with a big total pressure loss. In this case, the maximum entropy generation value is $122\,\mathrm{J\,kg^{-1}\,K^{-1}}$.

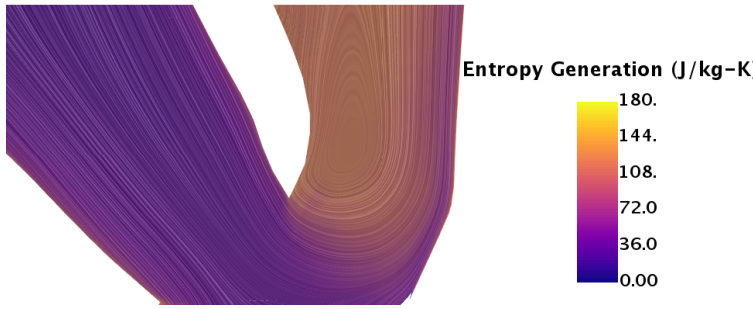

Figure 11. Interspace sudden expansion and recirculation for a case of *MFR* 1.

For quantifying the losses due to the sudden expansion at the junction of both flow branches, a model based on the Borda-Carnot sudden expansion equation could be used. The model employed is defined in Eq. 3, where ρ is the density, v the absolute velocity, K a constant to be adjusted and A_{in} and A_{out} the inlet and outlet interspace areas.

$$\Delta p_{SudExp} = K \cdot \rho \cdot v^2 \cdot (1 - A_{in}/A_{out}) \tag{3}$$

Another source of losses in the interspace found is the interaction of both flow branches. Each flow branch has its own conditions of pressure and velocity coming from its respective volute limb. If these conditions are different for each flow branch, there are another kind of total pressure change, apart from the sudden expansion produced by the pressure difference, that comes from the momentum exchange between flow branches.

Fig. 12 shows a velocity map in the interspace for a case with an *MFR* equal to 0.67. The difference of velocities between flow branches is noticeable. This difference produces a gradient of velocities in the normal direction of the flow and, more specifically, normal to the contact surface between flow branches. Since one flow branch momentum is higher than the other, when they are in contact, the flow branch with higher momentum will transmit some to the one with lower momentum.

So, the flow branch that has higher momentum will exhibit total pressure losses due to this momentum exchange between flow branches. However, the flow branch that has lower momentum will exhibit gains due to this momentum exchange between flow branches.

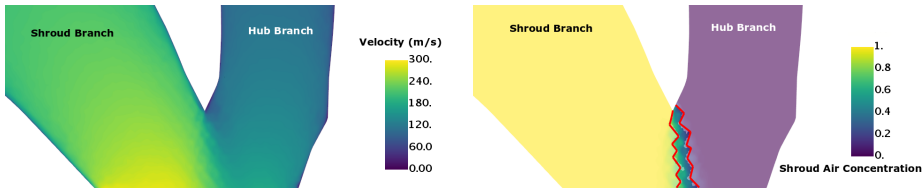

(a) Velocity map. **(b)** Contact surface between flow branches.

Figure 12. Velocity map and contact surface in a section at 90° from the tongue in the interspace for a case with an *MFR* equal to 0.67.

From Fig. 10, it can be observed that the flow from both branches does not mix with each other in the interspace and there is only a thin region where both flow branches have mixed. For inquiring in the losses due to the contact between flow branches, the contact surface between flow branches can be studied using again the shroud air concentration. So, the interspace region where the shroud air concentration is 0.5 ± 0.2 will be considered the contact surface, as remarked in red in Fig. 12b. This region is small, but it is where the exchange of momentum is produced.

This momentum exchange produced in the contact between flow branches is a turbulent phenomenon. So, turbulence parameters as the turbulent viscosity and the turbulent characteristic length can be studied in order to identify their effect on these losses. For calculating these parameters, the turbulent kinetic energy (k) and the specific dissipation rate (ω) are obtained for each simulated case in the interspace as the mean value of all its cells. Then, using the equations given by the $k-\omega$ SST model chosen in the current CFD simulations, the turbulent characteristic length and the turbulent viscosity can be computed. The turbulent characteristic length can be calculated following Eq. 4, being β^* a turbulent model coefficient and equal to 0.09. The turbulent viscosity can be calculated following Eq. 5, being ρ the density in the region. The momentum exchange and total pressure changes are expected to be proportional to the turbulent viscosity, defined in Eq. 5. Moreover, the momentum exchange between flow branches will be inversely proportional to the thickness of the contact surface region. This

thickness is of the same order of magnitude than the characteristic length of the bigger turbulent eddies, calculated in Eq. 4.

$$L_t = \frac{\sqrt{k}}{\beta^{*0.25} \cdot \omega} \tag{4}$$

$$\mu_t = \frac{\rho \cdot k}{\omega} \tag{5}$$

Fig. 13 shows respectively the turbulent characteristic length 13a and the turbulent viscosity 13b in the interspace for all simulated cases as the mean value of all its cells. From 13a, it can be concluded that the turbulent characteristic length is practically constant and independent of the *MFR* and reduced turbocharger speed conditions. However, the turbulent viscosity in 13b is independent of the *MFR* but not of the reduced turbocharger speed. In the simulated cases, increasing the turbocharger speed means increasing also the inlet pressure conditions and, thus, the density. Since the turbulent viscosity depends directly on the density, it will depend also directly on the reduced turbocharger speed.

As the thickness of momentum exchange region is relatively constant, the total pressure losses seem to be only a function of the difference between the flow branch velocities, size of contact area and turbulent viscosity, which seems to be a function of reduced turbocharger speed. The dependency of the turbulent viscosity on the reduced turbocharger speed can be explained by the direct correlation between the Reynolds number of the flow and the reduced turbocharger speed in the CFD simulations carried out: when the reduced turbocharger speed was increased, the mass flow and the Reynolds number were also increased. A model for predicting the effect of this momentum exchange region should depend on these effects. This model could be defined as in Eq. 6, where L_{CA} is the size of the contact area, v_h and v_s are the respective velocities of each branch at the interspace inlet and Z_{ME} is a variable to be adjusted that will include the turbulent viscosity effect.

$$\Delta p_{ME} = Z_{ME} \cdot L_{CA} \cdot (v_h - v_s)^2 \tag{6}$$

The effect of the sudden expansion and the momentum exchange between flow branches on the total pressure losses has been quantified and added to the passage losses that were previously shown in Fig. 9.

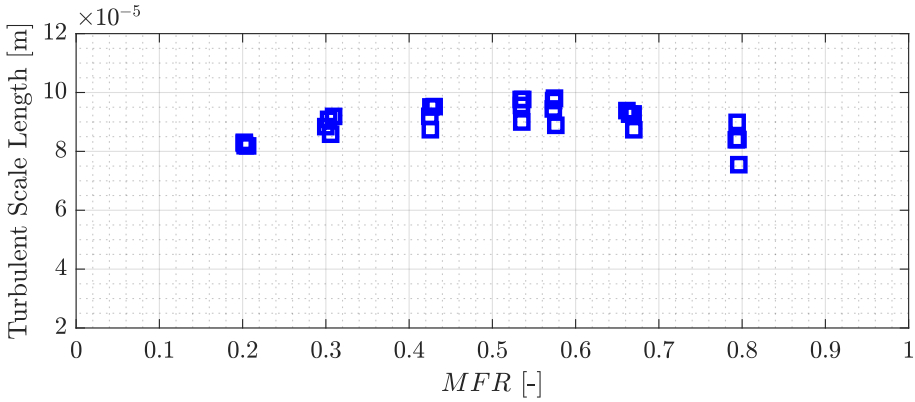

(a) Turbulent characteristic length.

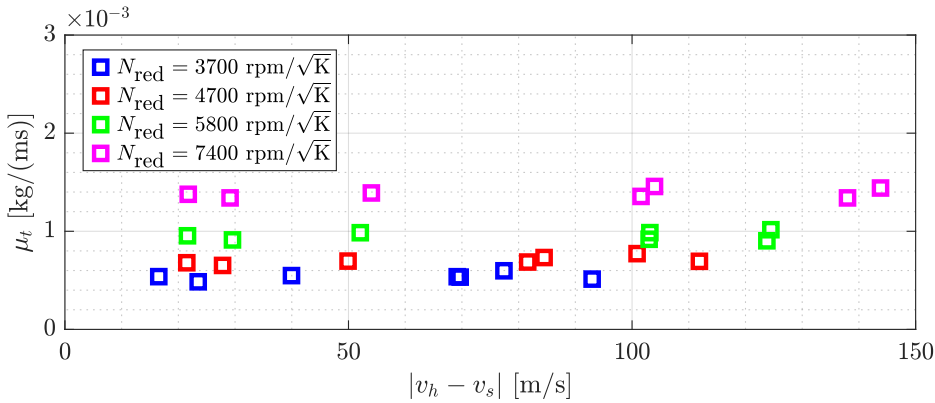

(b) Turbulent viscosity.

Figure 13. Interspace turbulence definition.

Then, all these modelled total pressure losses have been compared with the interspace total pressure losses obtained from the CFD simulations respectively for the hub branch and the shroud branch in Fig. 14. For obtaining the total pressure losses in the CFD simulations, the total pressure has been evaluated at the inlet and outlet areas corresponding to each flow branch, as defined in Galindo et al. [22]. The difference in total pressure losses between the CFD simulations and the correlations provided is shown in Fig. 14 over the bars if the models under-predict the total pressure losses and under 0 if the models over-predict the total pressure losses.

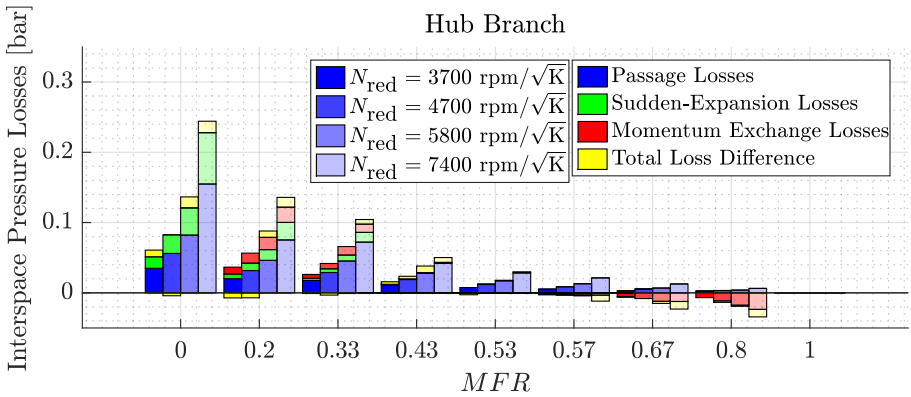

(a) Hub branch.

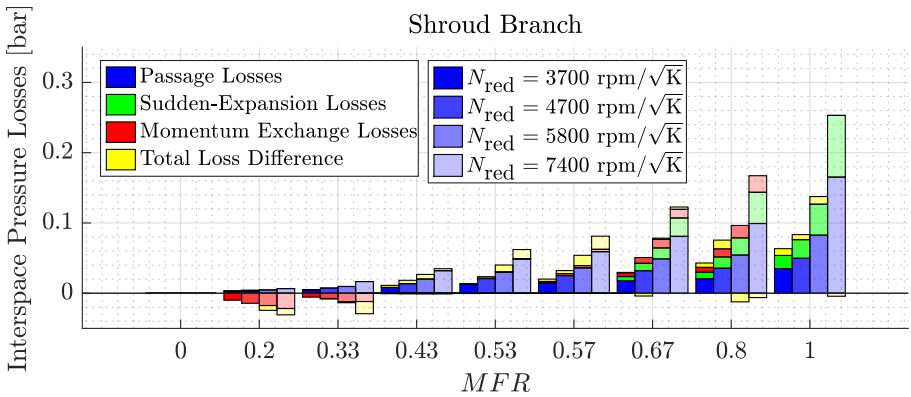

(b) Shroud branch.

Figure 14. Interspace total pressure losses.

Fig. 14 shows that the cases with the most significant losses are for partial admission conditions (*MFR* 0 for the hub branch and 1 for the shroud branch). This is due to the huge re-circulation from one volute to the other, as shown in Fig. 11, which is a considerable source of losses. The total interspace pressure losses diminish when the *MFR* value goes toward full admission conditions (*MFR*0.5) since the losses due to the sudden expansion at the junction of both volutes also diminish. However, the total pressure losses in the interspace continue diminishing when the flow branch studied has less mass flow rate than the other (*MFR* higher than 0.5 for the hub branch and lower than 0.5 for the shroud branch). In these cases is where the effect of the losses due to the momentum

exchange between flow branches are clearer. The total pressure losses can indeed become into gains in extreme values of *MFR* like 0.8 in the hub branch or 0.2 in the shroud branch.

Taking into account the losses due to the sudden expansion and the losses due to the momentum exchange between flow branches, the difference between the quantified pressure losses and the total pressure losses obtained from the CFD is better captured, especially for the unequal admission cases. It could represent up to 30 % of the total losses in the flow branch with more mass flow rate (*MFR* lower than 0.5 for the hub branch and higher than 0.5 for the shroud branch).

However, the most significant effect can be observed in the flow branch with less mass flow rate (*MFR* higher than 0.5 for the hub branch and lower than 0.5 for the shroud branch). In these cases, there are gains instead of losses and with the losses due to the momentum exchange between flow branches they can be explained and well captured. The authors of this manuscript have not found in the literature the inclusion of these effects in losses-based reduced order models for twin-entry turbines. These effects should be considered in these models for capturing correctly the pressure losses in twin-entry turbines.

4.3 Rotor Losses

Since the rotor is the mobile part of the twin-entry turbine, more complex phenomena arise in this region due to its motion. The main sources of losses typically considered in the literature for this region are those due to the inlet incidence and the friction and interaction with the blades walls [31]. Other authors have also considered the losses due to secondary flows like the tip losses [32]. However, the authors of this manuscript have not found any mention in the literature about considering the losses due to the exchange of momentum between flow branches in the rotor of twin-entry turbines. Moreover, the effect of the *MFR* value on the well-known losses of incidence, passage and secondary flows is also studied.

The rotor inlet incidence losses are produced when the inlet incidence relative velocity angle (β_3) is different from the optimum angle. In the previous section, it has been observed that the flow of each branch remains mainly separated in the interspace as the contact surface is small. So, in unequal admission conditions, the rotor inlet incidence angle will have two clearly different values along the blade height.

This effect can be observed in Fig. 15, where the entropy generation with relative velocity convolution lines in a radial-tangential plane is shown for an *MFR* value of 0.67 at two different blade heights. The two blade heights selected are at 10 % and at 90 % of the blade height, being each one clearly in the region where there is flow coming from only one branch (from the hub branch in the plane at 10 % and from the shroud branch in the plane at 90 %).

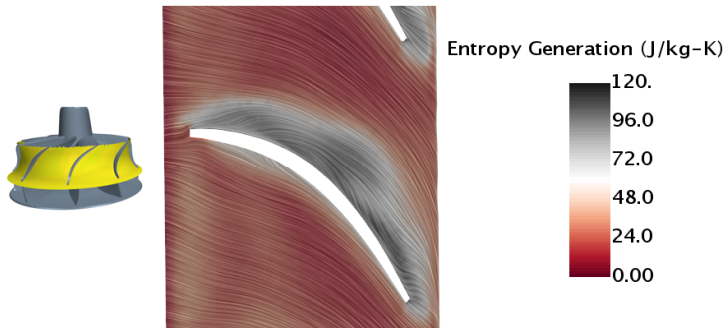

(a) At 90 % of the blade height, Shroud branch.

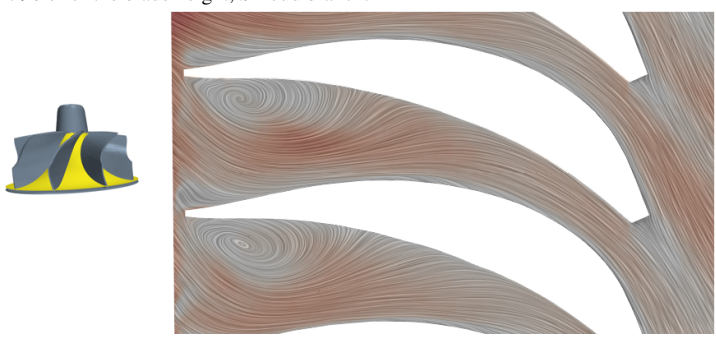

(b) At 10 % of the blade height, Hub branch.

Figure 15. Rotor inlet incidence angle effect on the entropy generation for an *MFR* equal to 0.67 at different blade heights.

The optimum angle for the twin-entry turbine studied is $-23.7°$. With this angle, the losses are minimized and the flow is aligned with the geometry, as it has been observed in the CFD simulations. In Fig. 15a, the rotor inlet incidence angle seems to be close to the optimum angle. However, in Fig. 15b there are greater recirculation regions with higher entropy generation, which is due to the rotor inlet incidence angle is farther from the optimum angle. This different flow behaviour along the

blade height for the same case is due to the different pressure and velocity conditions of each flow branch at the rotor inlet. With an MFR value of 0.67, the flow coming from the shroud branch has more kinetic energy at rotor inlet and, thus, its incidence angle is closer to the optimum. Meanwhile, the hub flow impacts the suction side of the blades, producing an important flow detachment in the pressure side.

The same flow behaviour is observed in cases with *MFR* values higher than 0.5, whereas the same behaviour but in the opposite branch is obtained in *MFR* values lower than 0.5. For cases near full admission conditions like with an *MFR* equal to 0.53, the rotor inlet incidence angle is similar across the whole blade height.

Thus, depending on the *MFR* value and the region of the blade height at the rotor inlet, the losses due to the rotor inlet incidence angle will change. The model proposed by Chen and Baines [33] can be useful for quantifying these losses if the incidence angle is calculated in each blade height region. The model employed is defined in Eq. 7, where w is the rotor inlet relative velocity, K a constant to be adjusted and β and β_{opt} the incidence angle and the optimum incidence angle.

$$\Delta p_{inc} = K \cdot w^2 \cdot (\sin\beta - \beta_{opt})^2 \tag{7}$$

The other main source of losses usually taken into account are the passage losses. These losses are also expected to vary with the *MFR* since the portion of rotor volume occupied by each flow branch varies with the *MFR*, as detailed in [22]. So, when the *MFR* value increase from 0 to 1, the passage losses increase in the shroud branch and diminish in the hub branch. For quantifying the passage losses in the rotor, a reasonable approximation is to use again the passage losses model proposed by Futral et al. [30] and shown in Eq. 2 since it is well validated in the literature.

Another kind of rotor losses typically considered in the literature are the tip losses. The phenomena that produce these losses have been well defined by other authors and the model used by Serrano et al. [23] for single-entry turbines can be used for quantifying these losses in twin-entry turbines. This model is defined in Eq. 8, where ρ is the density, w_- and w_+ are modelled velocities that depend on tip geometry and M_- and M_+ are modelled mass flow coefficients that also depend on tip geometry.

$$\Delta p_{tip} = \rho \cdot (M_- \cdot w_-^2 + M_+ \cdot w_+^2) \tag{8}$$

The losses due to tip secondary flows only affect the shroud flow branch in all values of *MFR* except the *MFR* 0, where there is only flow from the hub branch.

Fig. 16 shows the incidence, passage and tip losses quantified with the models proposed and their differences with the total pressure losses obtained from the CFD results in the rotor for each branch, respectively. Generally, the passage losses are the main contribution to the losses. The incidence losses are important where there is lower mass flow rate in the branch of study (*MFR* higher than 0.5 in the hub branch and lower than 0.5 in the shroud branch), but also a bit in partial admission conditions. The contribution of the tip losses is lower than the others, but still important for the shroud branch and the partial admission condition in the hub branch.

However, with all these losses taken into account, there are considerable differences in unequal admission conditions while in partial admission conditions and near full admission conditions these differences are lower. In the cases with lower mass flow rate in the branch of study (*MFR* higher than 0.5 in the hub branch and lower than 0.5 in the shroud branch), there is an over-prediction of the pressure losses while in the cases with higher mass flow rate in the branch of study there is an under-prediction of the pressure losses.

Thus, there is another source of losses in the rotor of twin-entry turbines that other authors have not taken into account yet, and it is the exchange of momentum between flow branches. As in the interspace, each flow branch has its own conditions of pressure and velocity and both flows arrive to the rotor inlet mainly separated, as shown in Fig. 12b.

Using again the shroud air concentration for following the mass fraction of the gas corresponding to the one entering through the shroud branch, the rotor contact surface between flow branches is considered where the shroud air concentration is 0.5 ± 0.2, as shown in Fig. 17 for a case with an *MFR* equal to 0.67. It can be noted that both flow branches are still separated, but the contact surface, which is highlighted in green in Fig. 17, becomes larger when the flow advances to the rotor outlet. Since one flow branch momentum is higher than the other, when they are in contact, the flow branch with higher momentum will transmit some of its momentum to the one with lower momentum. Hence, while the flow branch with higher momentum has losses due to this contact, the flow branch with lower momentum will exhibit gains, as it happened in the interspace.

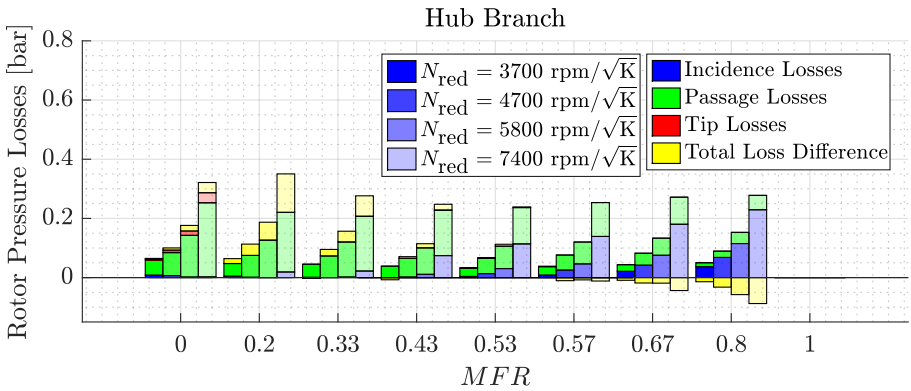

(a) Hub branch.

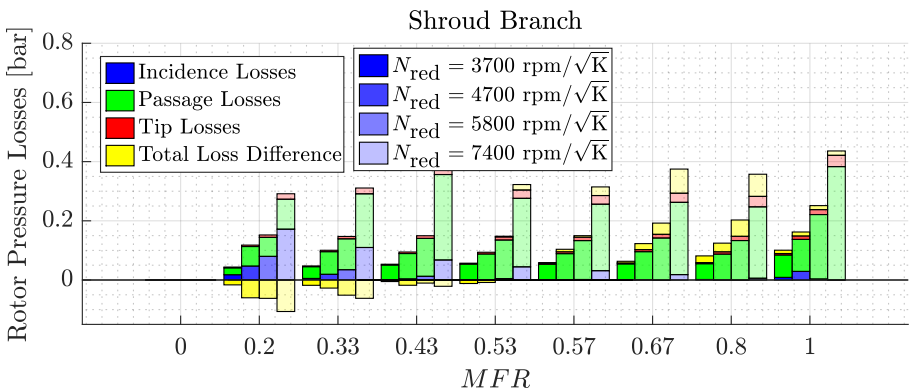

(b) Shroud branch.

Figure 16. Rotor total pressure losses quantification.

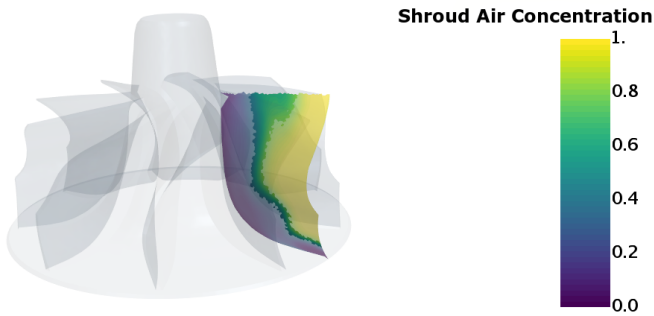

Figure 17. Shroud air concentration map in a middle channel surface of the rotor.

Since these losses are a turbulent phenomenon, the turbulent viscosity and the turbulent characteristic length can be studied to know their effect as it has been done in the interspace.

Fig. 18 shows respectively the turbulent characteristic length 18a and the turbulent viscosity 18b in the rotor as the mean value of all its cells for all simulated cases. Both the turbulent characteristic length and the turbulent viscosity in the rotor are practically constant with the *MFR*, but they depend on the reduced turbocharger speed. Again, the main effect is due to varying Reynolds numbers, as they are bigger with bigger reduced speeds in the cases studied. The different motion of the rotor with the reduced turbocharger speed can enhance some turbulent phenomena like flow detachments: this makes the turbulent characteristic length also dependent on the reduced turbocharger speed in the rotor.

So, the losses due to the momentum exchange between flow branches in the rotor depend on the difference between flow branches velocities, the size of the contact area between them, the pressure inlet conditions through the turbulent viscosity and other turbulent effects through the turbulent characteristic length. For quantifying these losses, a model similar to the one defined in the interspace losses section with Eq. 6 could be used.

For quantifying the effect of the losses due to the momentum exchange between branches, Fig. 19 shows the accumulated effect of all the pressure losses described and their differences with the total losses obtained from the CFD results for the hub branch 19a and the shroud branch 19b respectively.

The losses due to the momentum exchange between flow branches have no effect in partial admission conditions, where the gas comes from only one of the turbine intake ports. They have a small effect near full admission conditions where the pressure and mass flow rate conditions for each flow branch are similar. However, in unequal admission conditions, these losses have reduced a lot the under-prediction in the cases with higher mass flow rate in the branch of study (*MFR* lower than 0.5 for the hub branch and higher than 0.5 for the shroud branch). As these losses also take into account if the branch yields gains instead of losses, the over-prediction in the cases with lower mass flow rate in the branch of study (*MFR* higher than 0.5 for the hub branch and lower than 0.5 for the shroud branch) is also accurately captured.

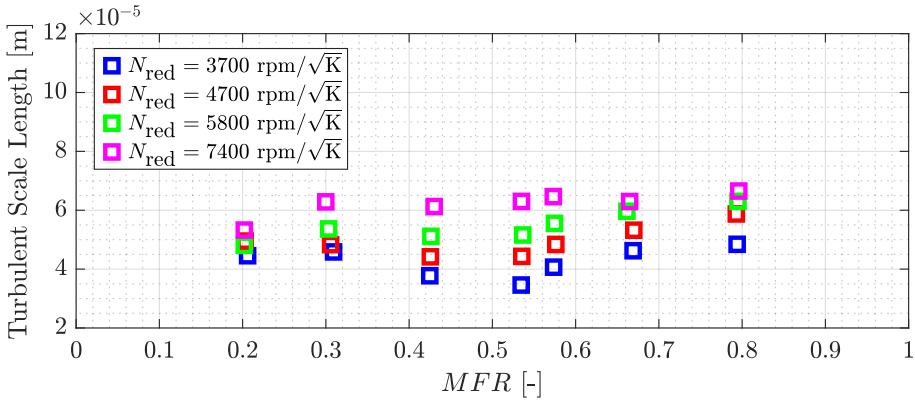

(a) Turbulent characteristic length

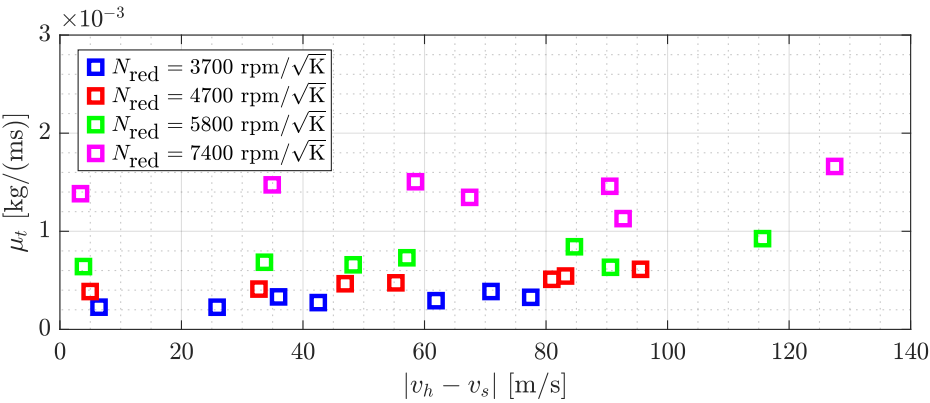

(b) Turbulent viscosity.

Figure 18. Rotor turbulence definition.

Thus, the losses due to the momentum exchange between flow branches allow to reduce the differences between the quantified pressure losses and the total pressure losses for unequal admission conditions, representing up to 25 % of the total pressure losses in some cases. As in the case of the interspace, these effects should be taken into account in losses-based reduced order models for twin-entry turbines.

4.4 Outlet Losses

The losses in this region are mainly produced due to the sudden expansion at the end of the rotor nut and at the outlet plenum as proposed by Palenschat et al. [31]. However, there are other losses that should be

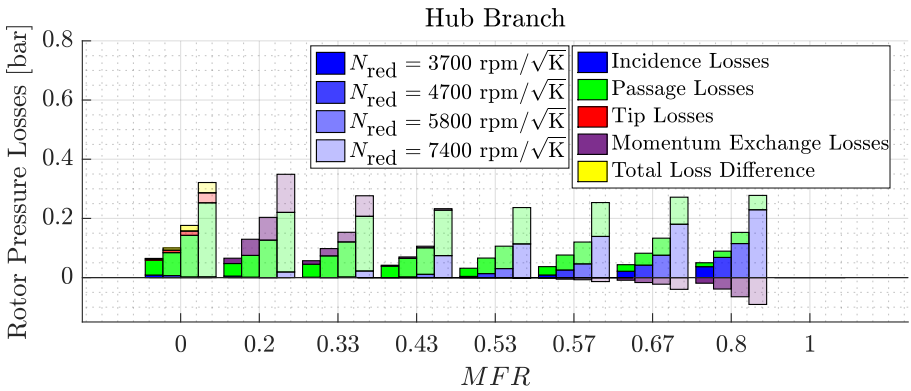

(a) Hub branch.

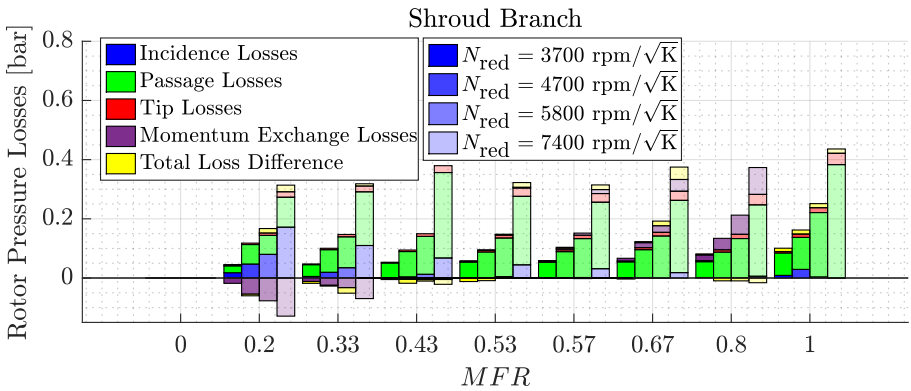

(b) Shroud branch.

Figure 19. Rotor total pressure losses.

taken into account that have not been considered by other authors. The full mixing of both flow branches is produced in the outlet, since they are not fully mixed within the rotor as shown in Fig. 17, and this is an extra source of total pressure losses. At the beginning of the outlet region, both branches are still separated. So, there could be also losses due to the exchange of momentum between flow branches in a thin region as in the interspace and rotor regions. The effect of these losses should be evaluated also in terms of *MFR*.

Two sudden expansions can be differentiated at the outlet. The first when the flow arrives at the end of the rotor nut. The second sudden expansion happens later in the flow direction when it arrives to the plenum where

the waste-gate is located. Both sudden expansions are expected to be the main source of losses in the outlet region. Fig. 20 shows a plane of the entropy generation with velocity convolution lines in the outlet region for a case with an *MFR* equal to 0.33 and a reduced turbocharger speed equal to $5800\,\mathrm{rpm\,K^{-0.5}}$.

There are large eddies just after the end of the rotor nut and an increase in the entropy generation. Large eddies can also be observed at the right side of the plenum where the waste-gate is located. There is additionally a smaller eddy at the left side of the plenum where there is a smaller sudden expansion. The losses due to sudden expansions could be quantified employing a model based on the sudden expansion Borda-Carnot equation, as already shown in the interspace losses section with Eq. 3.

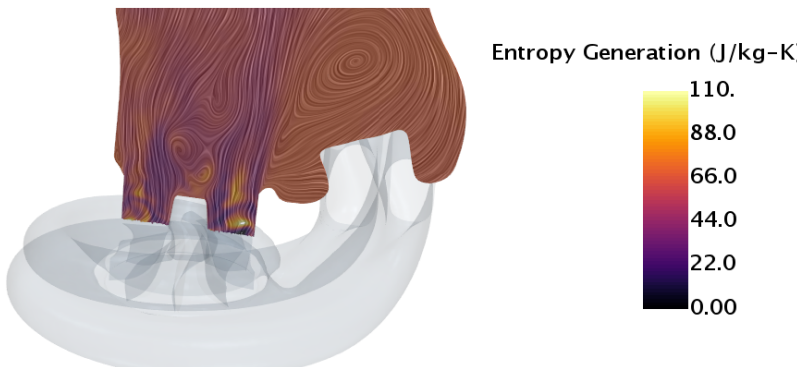

Figure 20. Entropy generation at the outlet region due to sudden expansions.

Fig. 21 shows the sudden expansion losses quantified with the model proposed and its differences with the total pressure losses obtained from the CFD results. In partial admission conditions, these differences are near 0 since the sudden expansions are the most significant phenomenon. Despite it captures most of the losses, there are still substantial differences in unequal admission conditions. The mixing losses become important in these cases and it should be taken into account. In addition, the losses due to the momentum exchange between branches could produce a small effect since at the beginning of the outlet region the flow branches are still separated.

The full mixing of both flow branches can be seen in Fig. 22 following the shroud air concentration for a case with an *MFR* equal to 0.53

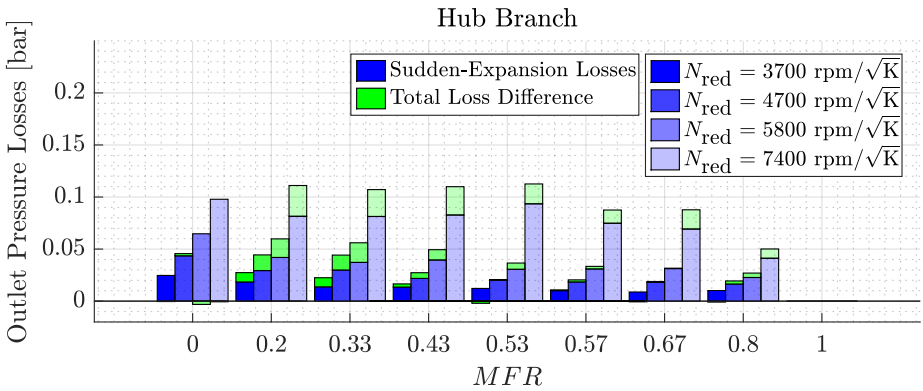

(a) Hub branch.

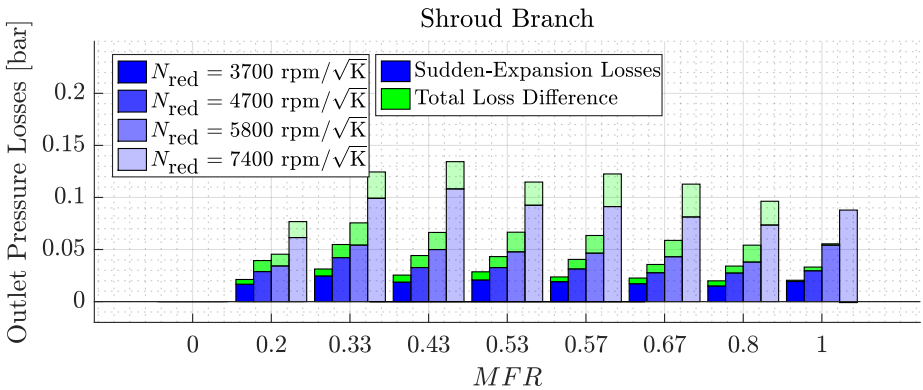

(b) Shroud branch.

Figure 21. Outlet sudden expansion pressure losses.

and a reduced turbocharger speed of $3700\,\mathrm{rpm\,K^{-0.5}}$. The highlighted region corresponds to values of the shroud air concentration equal to 0.5 ± 0.2. This mixing produces losses in the flow due to its turbulence behaviour. For quantifying these losses, a model based on the junction losses proposed by Winterbone and Pearson [34] could be used. The model employed is defined in Eq. 9, where ρ is the density, v is the absolute velocity at the outlet section, K a constant to be adjusted and AG is a parameter that depends on the outlet region geometry.

$$\Delta p_{mix} = K \cdot \rho \cdot v^2 \cdot AG \tag{9}$$

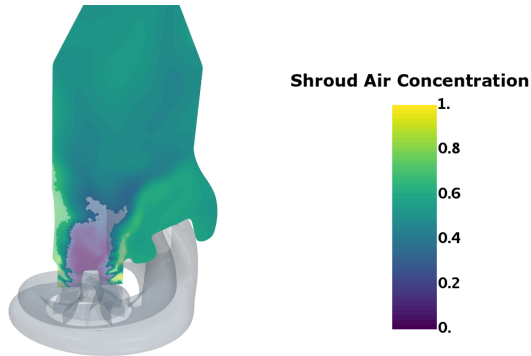

Figure 22. Shroud air concentration in the outlet region for a case with *MFR* 0.53

Despite the flow branches mix completely at the outlet, there is still a small region just at the rotor outlet where both flow branches are still separated as it can be observed in Fig. 22. Thus, there are also losses due to the exchange of momentum between flow branches. As in the interspace and the rotor, the flow branch with higher momentum will have losses and transmit some of its momentum to the flow branch with lower momentum which will exhibit gains.

For quantifying the effect of both the mixing losses and the losses due to the momentum exchange between branches, Fig. 23 shows the accumulated effect of all the pressure losses described and the differences with the total losses obtained from the CFD results for the hub branch 23a and the shroud branch 23b, respectively. These losses have no effect on partial admission conditions since there is only one flow branch, but they are important in unequal admission conditions.

The mixing losses are important in all unequal admission conditions cases, and it can represent up to 20 % of the total pressure losses in some cases. Thus, they should be taken into account in losses-based reduced order models for twin-entry turbines.

The losses due to the momentum exchange between branches have lower effect on the total losses and they represent less than 3 % of the total losses in the outlet for most cases. The region where the flow branches are still separated is small. The pressure and velocity conditions with which they arrive to the outlet are similar, so these losses are small. However, they could still be included in losses-based reduced order models.

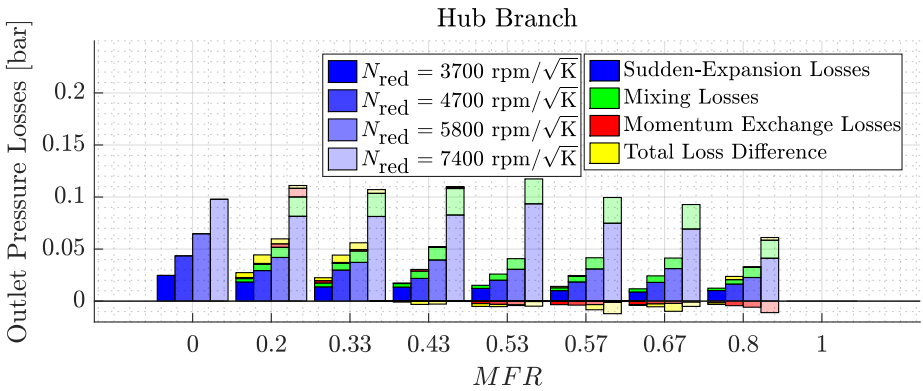

(a) Hub branch.

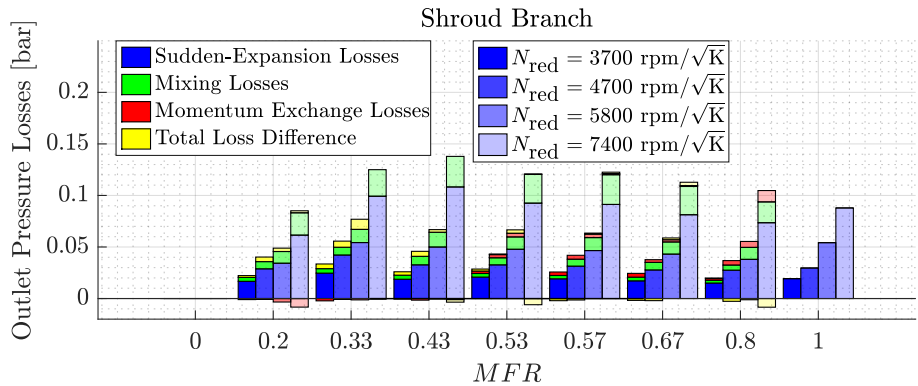

(b) Shroud branch.

Figure 23. Outlet total pressure losses.

4.5 Total Losses

Finally, all the quantified losses can be summed up to identify what they represent for the total twin-entry turbine losses. Fig. 24 shows the sum of each twin-entry turbine part quantified pressure losses and their differences with the total pressure losses in the hub branch 24a and the shroud branch 24b, respectively. It is observed that the over or under-predictions merely represent less than 8 % of the total pressure losses in the worst cases.

All pressure losses increase with the reduced turbocharger speed since, for the simulated cases, increasing the reduced turbocharger speed means

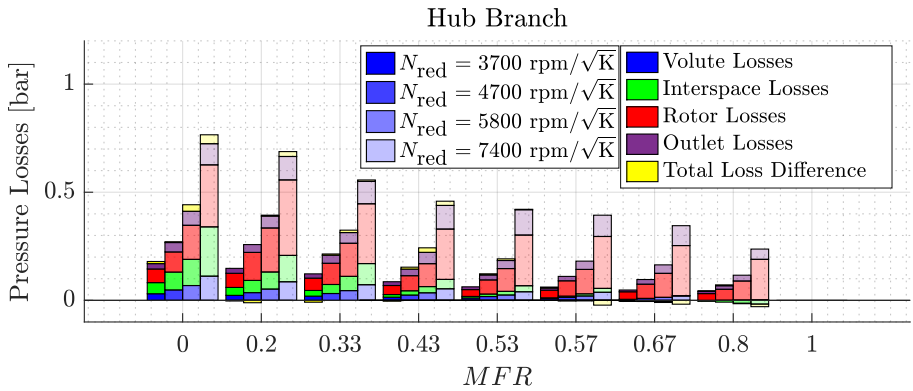

(a) Hub Branch.

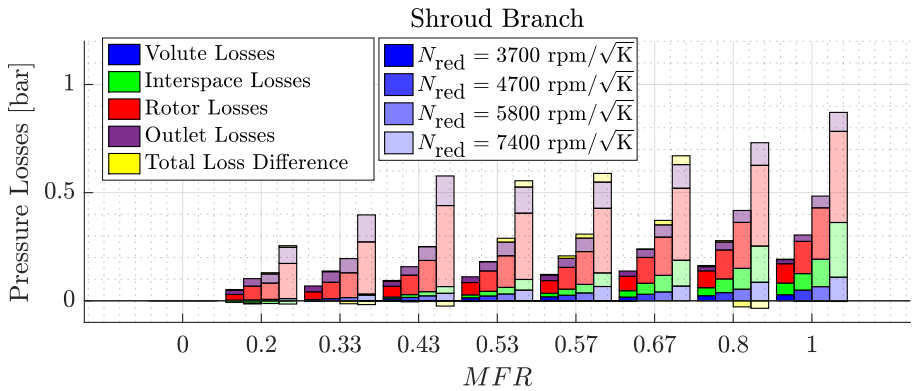

(b) Shroud Branch.

Figure 24. Pressure losses proportion of each turbine part.

increasing also the pressure ratio. However, the behaviour with the *MFR* needs to be also explained for each twin-entry turbine part.

The volute pressure losses decrease when the *MFR* goes from 0 to 1 for the hub branch and from 1 to 0 for the shroud branch. Since the mass flow rate in the branch also decreases it was the expected behaviour with the *MFR*.

The interspace losses depend strongly on the *MFR*. They can represent up to 30 % of the total pressure losses in cases with higher mass flow rate (*MFR* lower than 0.5 for the hub branch and higher than 0.5 for the shroud branch). These significant losses are due to the sudden expansion at the junction. However, these losses decrease and they can indeed become

into gains in cases with lower mass flow rate (*MFR* higher than 0.5 for the hub branch and lower than 0.5 for the shroud branch). There is no sudden expansion in these cases, and the momentum exchange between flow branches makes them to gain energy. These gains can become more significant than the other pressure losses in extreme unequal admission cases as with an *MFR* equal to 0.8 for the hub branch and an *MFR* equal to 0.2 for the shroud branch.

The rotor pressure losses have the biggest impact, representing more than 40 % of the total pressure losses in all cases, since a moving part can produce more complex and different phenomena than static parts. Their dependence with the *MFR* value is weaker than in the interspace losses. Their maximum variation is observed in extreme unequal admission conditions (*MFR* values of 0.2 or 0.8) when the momentum exchange between flow branches produces a notable effect.

The outlet losses are also important, and they can represent up to 25 % of the total pressure losses in some cases. They are practically constant with the *MFR* value since the main source of losses are the sudden expansions that are always present.

5 Conclusions

The current paper presents a CFD flow analysis in terms of *MFR* of the different twin-entry turbine losses focusing on the mixing phenomena at unequal admission conditions. These losses have been quantified to see the effect of each flow mechanism.

The losses in the interspace have a strong dependence on the *MFR* value. For *MFR* values far from full admission conditions, there is a sudden expansion at the junction of both branches that produces considerable losses. Also for *MFR* values far from full admission conditions, there is a substantial difference between the momentum of each branch that produces an exchange from the flow branch with higher momentum to the one with lower momentum. These last losses have no effect on partial admission conditions since there is only one flow branch, but they affect the cases with unequal admission conditions and can even produce gains instead of losses in the branch with lower mass flow rate.

There are also losses due to momentum exchange between flow branches in the rotor that make vary the rotor losses especially in extreme unequal admission conditions like at *MFR* values equal to 0.2 or 0.8.

The outlet losses are produced mainly by the sudden expansions at the rotor nut and the outlet plenum. However, in unequal admission conditions, the mixing losses are also important since it is the region where the main mix of both flow branches is produced. There are also losses due to the momentum exchange between flow branches in a thin region, but they cause a more limited effect than in the interspace or the rotor since the velocity conditions of each flow branch are similar at this point of the twin-entry turbine. Thus, these losses are practically constant with the *MFR* value.

Taking into account all these physical effects produced inside the twin-entry turbine and their variation with the *MFR*, the pressure losses are well captured. They can be explained better from a physical point of view while avoiding other empirical approximations. Moreover, the mixing phenomena and the momentum exchange between flow branches described help to understand the flow behaviour in unequal admission conditions cases. These cases are the most common in real engine operation and their phenomena were not completely properly understood.

This information is necessary for developing reliable mean line twin-entry turbine models based on losses calculations, and it should be representative for different twin-entry turbine sizes and configurations. Then, they could be combined with flow capacity models for improving the interpolation and extrapolation capacity of the current models. In future works, a loss-based model will be defined taking into account all the phenomena described in this paper and its extrapolation capacity will be proved.

Declaration of Competing Interest

None declared.

Acknowledgements

The authors wish to thank V. Ucedo for helping with the moulds, R. Carrascosa for his invaluable work during the experimental setup and campaign and P. Raga for his help with the setup of the CFD simulations. Finally, this work would not have been possible without the technical support of V. Lidó and J. Bustos of TODO-3D, who did a magnificent job scanning the turbine in 3D.

Funding

Nicolás Medina is partially supported through contract FPU17/02803 of Programa de Formación de Profesorado Universitario of Spanish Ministerio de Ciencia, Innovación y Universidades. This

work has been partially supported by the “Ayuda a Primeros Proyectos de Investigación” (PAID-06-18), Vicerrectorado de Investigación, Innovación y Transferencia de la Universitat Politècnica de València (UPV), València, Spain.

Nomenclature

Abbreviations

3D	Three-dimensional
CAD	Computer-aided design
CFD	Computational fluid dynamics
ER	Expansion ratio
GCI	Global convergence index
ICE	Internal combustion engine
MFR	Mass flow ratio
RANS	Reynols-averaged Navier-Stokes
URANS	Unsteady RANS

Roman letters

A	Area
AG	Mixing losses geometry parameter
K	Adjustable constant
k	Turbulent kinematic energy
L	Characteristic length
M	Torque
M_-	Modelled mass flow coefficient
M_+	Modelled mass flow coefficient
$\dot{m}$	Mass flow rate
N	Turbocharger speed
p	Pressure
v	Absolute velocity
w	Relative velocity
w_-	Modelled velocity
w_+	Modelled velocity
Y^+	Non-dimensional wall distance
Z	Adjustable variable

Greek letters

β	Relative velocity angle
β^*	Turbulent model coefficient
η	Apparent efficiency
μ	Viscosity
ω	Specific dissipation rate
ρ	Density

Subscripts and superscripts

3	Rotor inlet station
CA	Contact area
h	Hub branch
in	Inlet
inc	Incidence losses
ME	Momentum exchange between flow branches
mix	Mixing losses
opt	Optimum
out	Outlet
pass	Passage losses
red	Reduced
s	Shroud branch
SudExp	Sudden expansion losses
t	Turbulent
tip	Tip losses

References

1. European Comission. Emissions in the automotive sector, 2018. URL https://ec.europa.eu/growth/sectors/automotive/environment-protection/emissions_en.
2. Gong H, Ge Y, Wang J and Yin H. Light-duty vehicle emissions control: a brief introduction to the China 6 emissions standard. *Johnson Matthey Technology Review* 2017; 61: 269–278.
3. Environmental Protection Agency. Environmental protection agency control of air pollution from motor vehicles: Tier 3 motor vehicle emission and fuel standards, 2015. URL https://www.epa.gov/regulations-emissions-vehicles-and-engines/final-rule-control-air-pollution-motor-vehicles-tier-3.
4. International Council On Clean Transportation. India Bharat Stage VI emission standards, 2016. URL https://theicct.org/sites/default/files/publications/India%20BS%20VI%20Policy%20Update%20vF.pdf.
5. Broatch A, Olmeda P, Margot X and Gomez-Soriano J. A one-dimensional modeling study on the effect of advanced insulation coatings on internal combustion engine efficiency.

International Journal of Engine Research 2020; DOI:10.1177/1468087420921584.

6. Piscaglia F, Onorati A, Marelli S and Capobianco M. A detailed one-dimensional model to predict the unsteady behavior of turbocharger turbines for internal combustion engine applications. *International Journal of Engine Research* 2019; DOI:10.1177/1468087417752525.
7. Mohapatra C, Schmidt D, Sforozo B, Matusik K et al. Collaborative investigation of the internal flow and near-nozzle flow of an eight-hole gasoline injector (Engine Combustion Network Spray G). *International Journal of Engine Research* 2020; DOI:10.1177/1468087420918449.
8. Iacovano C, d'Adamo A, Fontanesi S, Di Ilio G an Krastev V. Application of a zonal hybrid URANS/LES turbulence model to high and low-resolution grids for engine simulation. *International Journal of Engine Research* 2020; DOI:10.1177/1468087420931712.
9. Netzer C, Seidel L, Ravet F and Mauss F. Assessment of the validity of RANS knock prediction using the resonance theory. *International Journal of Engine Research* 2020; 21: 610–621. DOI:10.1177/1468087419846032.
10. Sharma S, Broatch A, García-Tíscar J, Allport JM et al. Acoustic characteristics of a ported shroud turbocompressor operating at design conditions. *International Journal of Engine Research* 2020; 21 DOI:10.1177/1468087418814635.
11. Torregrosa A, García-Cuevas LM, Inhestern L and Soler P. Radial turbine sound and noise characterisation with acoustic transfer matrices by means of fast one-dimensional models. *International Journal of Engine Research* 2019; DOI:10.1177/1468087419889429.
12. Fraser N, Blaxill H, Lumsden G and Bassett M. Challenges for increased efficiency through gasoline engine downsizing. *SAE International Journal of Engines* 2009; 2: 991–1008. DOI: 10.4271/2009-01-1053.
13. Garret T, Newton K and Steeds W. Turbocharging and supercharging. *Motor Vehicle* 2000; : 556–589.
14. Aghaali H and Hajilouy-Benisi A. Experimental and theoretical investigation of twin-entry radial inflow gas turbine with unsymmetrical volute under full and partial admission conditions. In *Turbo Expo: Power for Land, Sea and Air*. ASME, pp. 1099–1107. DOI: 10.1115/GT2007-27807. Paper No: GT2007-27807.
15. Serrano JR, Arnau FJ, García-Cuevas LM, Soler P et al. An experimental method to test twin and double entry automotive turbines in realistic engine pulse conditions. *SAE Technical Paper* 2019; DOI:10.4271/2019-01-0319.
16. Romagnoli A, Martinez-Botas RF and Rajoo S. Steady state performance evaluation of variable geometry twin-entry turbine. *International Journal of Heat and Fluid Flow* 2011; 32(2): 477–489. DOI:10.1016/j.ijheatfluidflow.2010.12.002.
17. Jin J, Pan J, Lu Z, Wu Q and Xu L. Effect of balance valve on an asymmetric twin-scroll turbine for heavy-duty diesel engine *International Journal of Engine Research* 2020; 477–489. DOI:10.1177/1468087420930162.
18. Brinkert N, Sumser S, Weber S, Fieweger K et al. Understanding the twin scroll turbine: flow similarity. *Journal of Turbomachinery* 2013; 135: 021039. DOI:10.1115/1.4006607.
19. Xue Y, Yang M, Martinez-Botas RF, Romagnoli A and Deng K. Loss analysis of a mix-flow turbine with nozzled twin-entry volute at different admissions. *Energy* 2019; 166: 775–788. DOI:10.1016/j.energy.2018.10.075.

20. Cerdoun M and Ghenaiet A. Unsteady behaviour of a twin entry radial turbine under engine like inlet flow conditions. *Applied Thermal Engineering* 2018; 130: 93–111. DOI: 10.1016/j.applthermaleng.2017.11.001.
21. Chiong MS, Rajoo S, Martinez-Botas RF and Costall AW. Engine turbocharger performance prediction: One-dimensional modelling of a twin entry turbine. *Energy Conversion and Management* 2012; 57: 68–78. DOI:10.1016/j.enconman.2011.12.001.
22. Galindo J, Serrano JR, García-Cuevas LM and Medina N. Experimental and computational analysis of the flow passing through each branch of a twin-entry turbine. *14th International Conference on Turbochargers and Turbocharging* 2020; .
23. Serrano JR, Arnau FJ, Garcia-Cuevas LM and Inhestern LB. An innovative losses model for efficiency map fitting of vaneless and variable vaned radial turbines extrapolating towards extreme off-design conditions. *Energy* 2019; 180: 626–639. DOI:10.1016/j.energy.2019.05.062.
24. Serrano JR, Arnau FJ, García-Cuevas LM and Samala V. A robust adiabatic model for a quasi-steady prediction of far-off non-measured performance in vaneless twin-entry or dual-volute radial turbines. *Applied Sciences* 2020; 10(1955). DOI:10.3390/app10061955.
25. Galindo J, Navarro R, García-Cuevas LM, Tarí D et al. A zonal approach for estimating pressure ratio at compressor extreme off-design conditions. *International Journal of Engine Research* 2019; 20(4): 393–404. DOI:10.1177/1468087418754899.
26. Serrano JR, Arnau FJ, García-Cuevas LM and Soler P. Experimental validation of a one-dimensional twin-entry radial turbine model under non-linear pulse conditions. *International Journal of Engine Research* 2021; Volume: 22 issue: 2, page(s): 390–406 DOI:10.1177/1468087419869157.
27. Serrano JR, Arnau FJ, García-Cuevas LM, Samala V and Smith L. Experimental approach for the characterization and performance analysis of twin entry radial-inflow turbines in a gas stand and with different flow admission conditions. *Applied Thermal Engineering* 2019; 159. DOI:10.1016/j.applthermaleng.2019.113737.
28. Roache PJ. Perspective: A method for uniform reporting of grid refinement studies. *Journal of Fluids Engineering* 1994; 116(3): 405–413. DOI:10.1115/1.2910291.
29. Galindo J, Hoyas S, Fajardo P and Navarro R. Set-up analysis and optimization of CFD simulations for radial turbines. *Engineering Applications of Computational Fluid Mechanics* 2013; 7: 441–460. DOI:10.1080/19942060.2013.11015484.
30. Futral S, Wasserbauer C, Aeronautics USN and S Administration. Off-design performance prediction with experimental verification for a radial-inflow turbine. Technical report, NASA TN D-2621, 1965. URL http://books.google.es/books?id=N1kzLAHfK-IC.
31. Palenschat T, Mueller M, Rajoo S, Chiong S et al. Steady-state experimental and meanline study of an asymmetric twin-scroll turbine at full and unequal and partial admission conditions. *SAE Technical Paper* 2018; DOI:10.4271/2018-01-0971.
32. Hajilouy A, Rad M and Shahhosseini MR. Modeling of twin-entry radial turbine performance characteristics based on experimental investigation under full and partial admission conditions. *Scientia Iranica* 2009; 281–290.
33. Chen H and Baines NC. The aerodynamic loading of radial and mixed-flow turbines. *International Journal of Mechanical Sciences* 1994; 36: 63–79. DOI:10.1016/0020-7403(94)90007-8.

34. Winterbone DE and Pearson RJ. *Theory of engine manifold design: wave action methods for IC engines*. Professional Engineering Pub., 2000. ISBN 978-1-86058-209-7.